

Materials Advances through Aberration-Corrected Electron Microscopy

S.J. Pennycook, M. Varela, C.J.D. Hetherington, and A.I. Kirkland

Abstract

Over the last few years, the performance of electron microscopes has undergone a dramatic improvement, with achievable resolution having more than doubled. It is now possible to probe individual atomic sites in many materials and to determine atomic and electronic structure with single-atom sensitivity. This revolution has been enabled by the successful correction of the dominant aberrations present in electron lenses. In this review, the authors present a brief overview of these instrumental advances, emphasizing the new insights they provide to several areas of materials research.

Keywords: electron energy loss spectroscopy (EELS), scanning transmission electron microscopy (STEM), transmission electron microscopy (TEM).

Introduction

Richard Feynman is widely associated with the nanoscience revolution as a result of his prophetic lecture "There's Plenty of Room at the Bottom," given in 1959.¹ Less well known is that, in the same lecture, he challenged us to "improve the resolution of the electron microscope by 100 times," his goal being to "just look at the thing." At the time of the lecture, it was understood that the resolution of the electron microscope was fundamentally limited by the intrinsic spherical aberration (by which rays far from the optical axis are over-focused) in the primary, image-forming magnetic objective lens. This spherical aberration is unavoidable with rotationally symmetric magnetic fields, and Feynman's response was simply "why must the field be symmetric?" Today, sophisticated electron-optical components are available which break this rotational symmetry, correcting spherical aberration and leading to higher resolution. The impact of these correctors on electron microscopy is evident from Figure 1, which shows the improvement in resolution from the era of optical microscopy to the present, although we

are not yet close to Feynman's challenge of 0.01 nm. The major reason that it has taken more than four decades to achieve this is the requirement for sophisticated computer control to measure the aberrations present and to iteratively adjust the necessary lens currents. As an example, optimization of the 12 independent third-order aberrations (including the spherical aberration) requires precise control of 40 or more optical elements. However, the current generation of correctors readily achieve this and are able to correct the electron wave front to a degree of perfection better than a quarter wavelength (~ 0.5 pm) over $70 \mu\text{m}$.

There are presently two designs of aberration corrector available for electron microscopes produced by Nion Co.³ and by CEOS GmbH.⁴ The former has been exclusively used in scanning transmission electron microscopy (STEM), whereas the latter has been used in both STEM and in conventional transmission electron microscopy (CTEM). Although the optical design of these two systems differs, it is important to appreciate that both correct only for the

geometric aberrations (of which spherical aberration is illustrated in Figure 2b) in the optical system through the use of non-round elements. Chromatic aberrations (Figure 2c) have so far only been successfully corrected in the scanning electron microscope (SEM),⁵ which operates at significantly lower accelerating voltages.

STEM or CTEM?

In CTEM, a near-parallel electron beam illuminates a thin sample, and the emerging scattered waves are focused by the objective lens to form an image, as shown in Figure 3a, with all image points being recorded simultaneously. In STEM, the incident beam is focused to a fine probe which is scanned across the sample with detectors arranged to record various signals, as shown in Figure 3b; in this mode, image points are obtained sequentially. CTEM, with its parallel recording, is therefore ideal for capturing specific signals rapidly from large fields of view, whereas STEM is optimal for extracting maximum information from a single point by detecting multiple signals (such as bright- and dark-field images or energy loss spectra) simultaneously. However, it is only relatively recently that both modes have become available on a single microscope column with anything approaching an optimum level of performance.

These two modes of operation may at first sight seem entirely different. In STEM, the primary focusing and aberration correction takes place before the specimen, whereas in CTEM it occurs after the

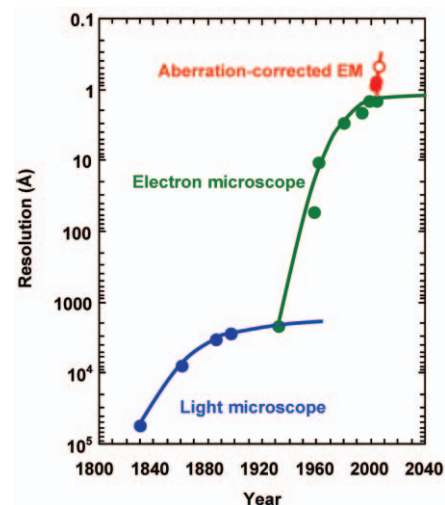


Figure 1. The evolution of resolution in microscopy (after H. Rose, adapted from Reference 2). The open circle is the predicted resolution for the next-generation fifth-order correctors currently under development.

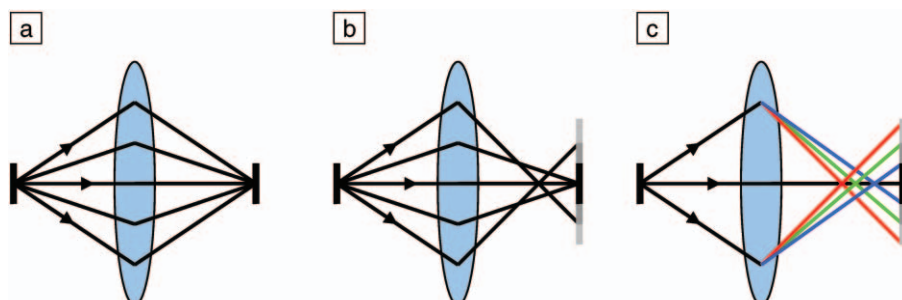


Figure 2. Illustration of certain lens aberrations. (a) A perfect lens focuses a point source to a single image point. (b) Spherical aberration causes rays at higher angles to be overfocused. (c) Chromatic aberration causes rays at different energies (indicated by color) to be focused differently.

specimen. However, Figure 3 illustrates that the two modes of operation are closely related. For bright-field imaging, with equivalent apertures before and after the specimen, the only difference between the two geometries is the ray direction. As a bright-field image is formed primarily from elastic scattering, which is independent of the direction of ray propagation, the two microscopes should give identical bright-field image contrast, and this indeed is the case. STEM is much less efficient than CTEM for image recording in bright-field because of its sequential acquisition and the low current that can be

focused into a small (uncorrected) probe. Uncorrected STEM bright-field images are hence inherently noisy, and the normal STEM imaging mode therefore uses an annular dark-field (ADF) detector that collects a large fraction of the scattered electrons. However, aberration correction in STEM significantly improves the collection efficiency for bright-field images such that they are no longer dominated by noise.

The primary imaging mode in CTEM is therefore bright-field, whereas in STEM it is ADF, or high-angle ADF (HAADF), for which the central hole in the detector is expanded. This HAADF image is also com-

monly referred to as a Z-contrast image, since at high angles the scattered intensity varies approximately as Z^2 , where Z is the atomic number.

These two modes also differ fundamentally in the mechanism by which the image contrast is obtained. In bright-field CTEM, the coherent phase-contrast image represents an interference pattern between the beams reaching the detector, and hence the contrast depends on the relative phases of these. In STEM, the HAADF detector integrates a large number of diffracted beams, and the incoherent Z-contrast image represents the total scattered intensity falling on the detector.

Phase contrast depends sensitively on the relative phases of the contributing diffracted beams, which depend in turn on the specimen thickness and atomic number and on the lens aberrations. These images therefore show complex contrast changes as a function of thickness and microscope operating conditions and in general require image simulation for interpretation in terms of the specimen structure. However, the advantage of coherent imaging is its efficient use of electrons. As an example, if we assume a specimen that generates a diffracted beam with an amplitude 10% that of the incident beam, then when the microscope objective lens is set to optimally interfere the diffracted beam with the unscattered beam, an image contrast of almost 20% results. Conversely, if we directly measure the intensity of the diffracted beam, we obtain an intensity of only 1% that of the incident beam for incoherent image formation.

From a materials perspective, the strength of phase-contrast imaging is its efficient exploitation of weak scattering through interferometric imaging, which makes it ideal for recording images of light, thin materials such as carbon nanotubes. For thicker specimens, the same efficient exploitation of weak scattering leads to artifacts that arise from interference between diffracted beams. Z-contrast images do not suffer from such artifacts and have the simple characteristics of an incoherent image (as for an optical camera), showing no contrast reversals (during which image features change from black to white with focus) and thus allowing optimum focus to be determined by the sharpest image. However, they do not make such efficient use of the incident electrons; hence, this mode is more suitable for thicker specimens or higher- Z materials. A good example of the different nature of these two types of image is shown in Figure 4, which compares two focal series of images of SrTiO_3 recorded in bright-field phase contrast and Z-contrast

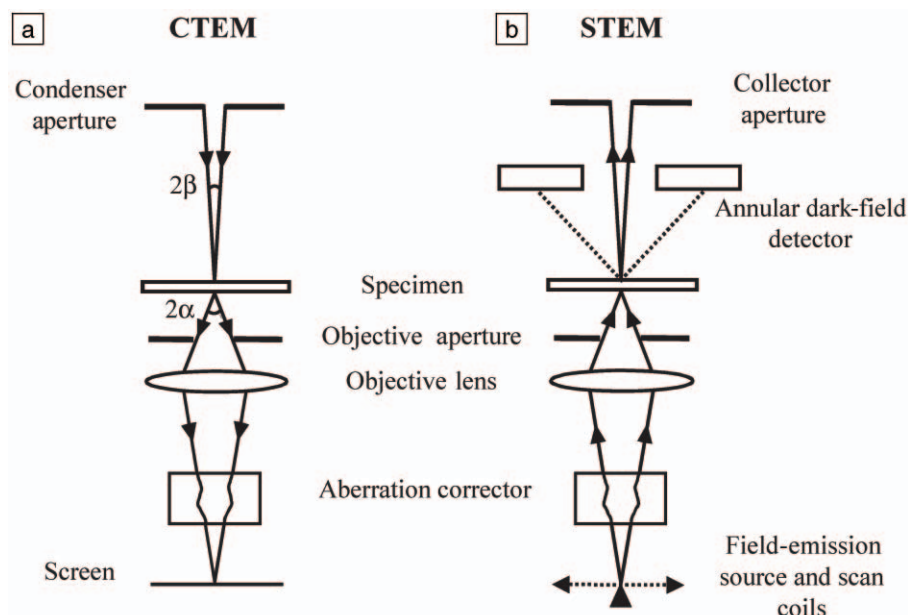


Figure 3. Ray diagrams showing the important optical elements for (a) conventional transmission electron microscopy (CTEM) and (b) scanning transmission electron microscopy (STEM). The CTEM image is obtained in parallel; the STEM image is obtained pixel-by-pixel by scanning the probe. The diagrams are shown with the electron source at the top for CTEM and at the bottom for STEM, to show the reciprocal nature of the optical paths. STEM also provides simultaneous annular dark-field imaging. Actual microscopes have several additional lenses, and the beam-limiting aperture positions may differ.

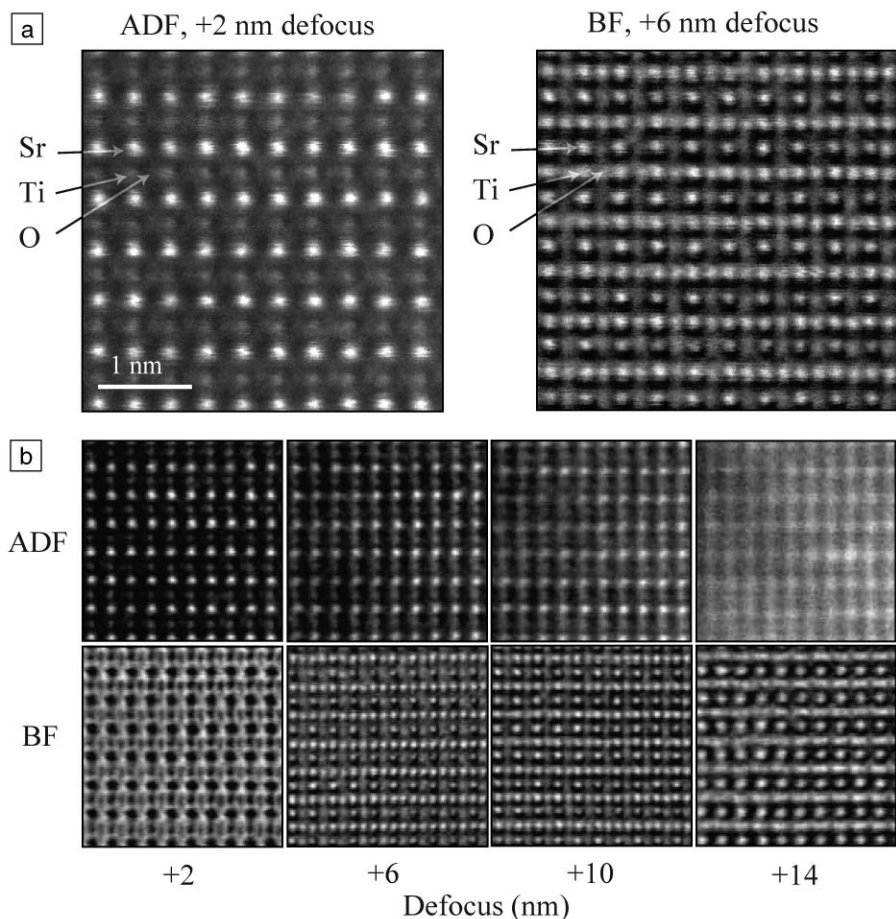


Figure 4. Comparison of incoherent and coherent imaging of SrTiO_3 in the $\langle 110 \rangle$ projection using a 300-kV HB603U STEM (VG Microscopes) with a Nion aberration corrector. A defocus series was taken using annular dark-field (ADF) and coherent bright-field (BF) detectors simultaneously. Positive defocus values indicate an overfocus. (a) At optimum focus, the ADF image shows Z-contrast, with O barely visible, while the phase-contrast BF image shows the O columns with high contrast. (b) Sequential frames from the focal series with 4-nm steps from the position of optimum ADF defocus, showing how the incoherent ADF image contrast slowly blurs while the phase-contrast image shows rapidly changing, complex variations in contrast. All images are raw data and show some instabilities. Microscope parameters are optimized for the smallest probe. (Courtesy of M.F. Chisholm, A.R. Lupini, and A. Borisevich.) This example shows that aberration correction provides more than just resolution improvement. In this case, it provides improved image contrast, allowing the detection of the light O columns in the presence of the adjacent heavy columns.⁶

modes. The images are obtained by STEM using simultaneous detection and hence show identical areas of a specimen. The phase-contrast images labeled bright-field (BF) in Figures 4a (right) and 4b (lower panel) are equivalent to those obtained using aberration-corrected CTEM, apart from the visible instabilities arising from environmental disturbances affecting the probe. The Z-contrast images labeled annular dark-field (ADF) in Figures 4a (left) and 4b (upper panel) show the expected Z dependence, with Sr atom columns appearing brightest, Ti less bright, and O columns barely observable above the

background noise. However, although the phase-contrast image changes rapidly with defocus, at optimum focus it highlights the weakly scattering O columns very clearly.

Aberration correction in CTEM images also leads to improvements in interpretable resolution and to reduced image delocalization, in which the structural information extends beyond the physical boundaries of the specimen. In the absence of spherical aberration, the point-to-point resolution of the image is extended out to the limits imposed by the partial coherence of the illumination; using 200-kV

microscopes, such as the JEM2200FS in Oxford,⁷ the point-to-point resolution is improved to ~ 0.1 nm from an uncorrected value of ~ 0.2 nm. The ability to tune the spherical aberration also provides both optimum phase-contrast imaging at small negative values of the spherical aberration and pure amplitude-contrast imaging at zero value,⁸ a mode which is not accessible in an uncorrected instrument. Information delocalization arising from the presence of aberrations in an uncorrected microscope is also substantially reduced, with particular benefits to the imaging of surfaces, boundaries, and other aperiodic features.

Mention should also be made of indirect methods that deconvolve the effects of aberrations from a series of CTEM images to leave the complex wave function at the exit plane of the specimen.⁹ This procedure can be usefully applied not only to uncorrected CTEMs but also to CTEMs fitted with aberration correctors to remove the effects of residual aberrations and to compensate for higher-order aberrations that cannot be corrected directly.

STEM aberration correction also enables substantial gains in performance in electron energy loss spectroscopy (EELS), due to the availability of smaller probes containing the same current. More current is thus placed down the atom column of interest with less wasted illuminating neighboring columns. We therefore win twice, gaining signal from the column of interest and reducing unwanted signal arising from overlap with neighboring columns. Overall, the net gain using current corrected STEM instruments is sufficient to allow a single atom to be identified spectroscopically within a single atomic column, as shown in Figure 5.

Case Studies in Materials with Aberration-Corrected STEM High- T_c Superconductors

While the detailed mechanism underlying high- T_c superconductivity (HTCS) in the highly anisotropic copper oxides remains elusive, it is generally accepted that superconductivity takes place in the CuO_2 planes, and atomic-resolution EELS gives direct proof for this in real space. Figure 6 shows a Z-contrast image of a $\text{YBa}_2\text{Cu}_3\text{O}_{7-x}/\text{PrBa}_2\text{Cu}_3\text{O}_7$ (YBCO/PBCO) superconducting/insulator (S/I) interface. In YBCO, the CuO plane containing the Cu-O chains is the lightest in the unit cell and is located further from the BaO plane than the CuO_2 layer. It therefore appears significantly darker in the Z-contrast image, while BaO planes appear brightest. The CuO_2 layers, together with the intermediate Y plane, are sandwiched between

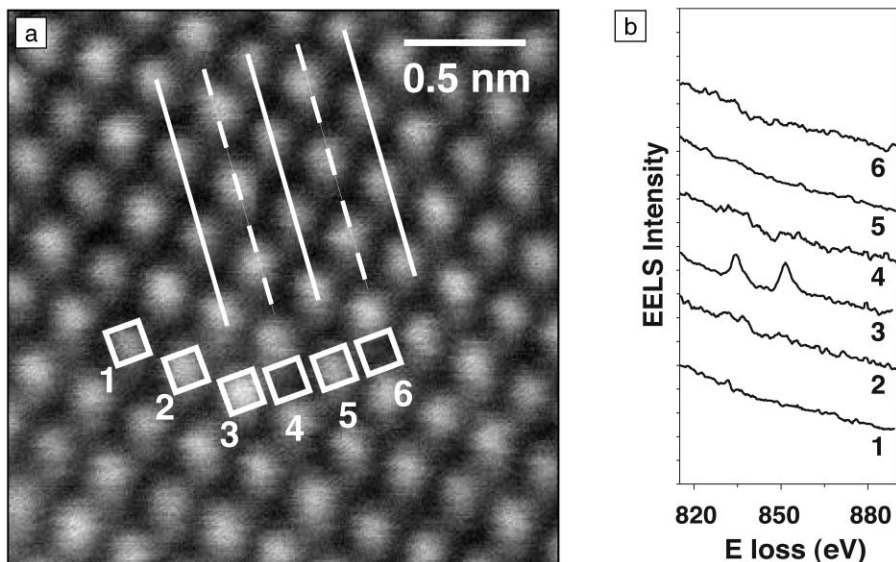


Figure 5. Spectroscopic identification of an individual atom in its bulk environment by electron energy loss spectroscopy (EELS). (a) Z-contrast image of CaTiO_3 , showing traces of the CaO and TiO_2 {100} planes as solid and dashed lines, respectively. A single La dopant atom in column 3 causes this column to be slightly brighter than other Ca columns, and EELS from it shows a clear La $M_{4,5}$ signal. (b) Moving the probe to adjacent columns gives reduced or undetectable signals.¹⁰

them. For this sample, the dopant level in the superconductor was measured by placing the electron beam at each atomic plane and acquiring EELS. For HTCS materials, the oxygen $2p$ bands lie very close to the Fermi energy, and the oxygen K edge, which results from exciting transitions from the oxygen $1s$ core level to the

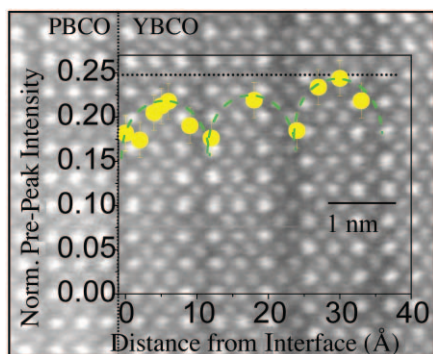


Figure 6. (Background) Z-contrast image of a (right/left) YBCO/PBCO interface. The interface position is marked with a vertical dotted line. The overlay graph (yellow filled circles) shows the normalized pre-peak intensity from the O K edge (i.e., density of holes) within the YBCO as a function of distance to the interface. The horizontal dotted line marks the hole concentration in bulk YBCO for reference.

$2p$ bands, can be used to probe the occupancy of the latter, thus giving a measure of the carrier density in the superconductor.^{11,12} The pre-peak in the O K edge contains most of the O $2p$ band contributions, and the hole density can be quantified by fitting the area under the pre-peak to a Gaussian function and normalizing with the area under the main body of the edge. Interestingly, EELS measurements in these samples show a spatial oscillation of the density of holes with a period equal to the lattice parameter, $c = 11.7 \text{ \AA}$. The hole density decreases on the CuO_2 planes, while it increases on the Cu chains, while it increases on the CuO_2 planes to almost the bulk value. Corresponding changes are also observed in the Cu L edge, which shows a corresponding modulation of the Cu formal oxidation state. This data is consistent with a +2 oxidation state in the CuO_2 planes and closer to +1 in the Cu chains. Hence, these measurements provide direct proof that the holes responsible for superconductivity are localized within the CuO_2 planes.¹³

Charge Ordering in Manganese Perovskites

Manganites are known to exhibit unusual lattice, electronic, and magnetic properties.¹⁴ In particular, within some regions of their phase diagrams, a form of spatial modulation known as the charge-ordered state is found. These phases are insulating and often antiferromagnetic, so

understanding the origin of this phenomenon may provide a key to the origin of ferromagnetism and colossal magnetoresistance (CMR)^{15,16} in these materials. CMR materials have a chemical formula $A_x\text{B}_{1-x}\text{MnO}_3$, where A is a trivalent cation (La, Nd, Bi, Pr) and B is a divalent cation (Sr, Ca, Ba). The resulting mixed-valence state within the Mn sublattice produces a complex electronic structure. The current view of this structure is that a fraction of the $1-x$ Mn ions per unit cell are in a +4 formal oxidation state, with a $3d^3$ electronic configuration ($t_{2g}^3e_g^0$ symmetry), while the rest have a $3d^4$ configuration ($t_{2g}^3e_g^1$). It has been suggested that the so-called charge-ordered (CO) state arises from a stable spatial ordering of the e_g electrons, so that the Mn sublattice is no longer a homogeneously mixed state. Atomic-resolution EELS is ideally suited for studying the electronic properties of solids with atomic resolution in real space, independent of the small lattice relaxations that contribute to superlattice reflections in diffraction methods.

Figure 7a shows a Z-contrast image of a $\text{Bi}_x\text{Ca}_{1-x}\text{MnO}_3$ (BCMO) manganite along the pseudocubic projection with $x = 0.37$. For this composition, the ordering temperature is above room temperature,¹⁷ and Figure 7b shows the dependence of the Mn oxidation state, with position x in angstroms, measured from the ratio of the Mn L_2 to L_3 peaks. The Mn oxidation state exhibits a modulation with a periodicity around 12 \AA ,¹⁸ with one in three Mn columns having a $3d^4$ atomic configuration. This stripe geometry determined from EELS is perfectly consistent with the

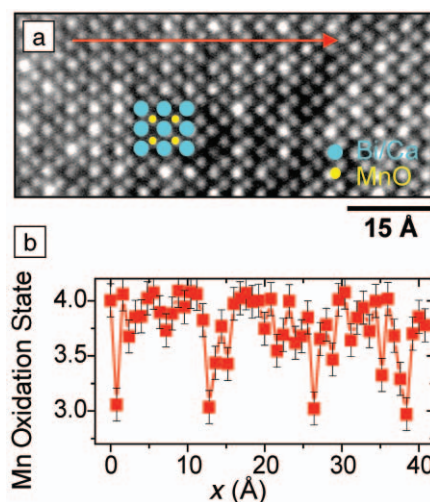


Figure 7. (a) Z-contrast image of a BCMO sample along the pseudocubic zone axis. (b) Manganese oxidation state along the red arrow in (a).

macroscopically averaged periodicity observed in electron diffraction,¹⁸ showing that the electronic striping is structural in origin.

Location of Rare-Earth Atoms in Ceramic Grain Boundaries

Rare-earth elements are frequently used in the preparation of Si_3N_4 ceramics to promote the growth of needlelike grains, thereby improving the toughness of the material. In the processed ceramic, the Si_3N_4 crystals are separated by ~ 1 -nm-thick amorphous films or larger glass pockets, and the additive rare-earth atoms are found at the prismatic $\{100\}$ crystal–amorphous interfaces, suggesting that their presence may have an influence on the growth kinetics. Furthermore, the average grain anisotropy of the ceramic varies according to the type of rare-earth element used. Determination of the location of different rare-earth atoms at the interface is therefore essential in clarifying their role in ceramic formation.^{19–21}

This problem lends itself to Z-contrast imaging, as the rare-earth atoms La ($Z = 57$) and Lu ($Z = 71$) have high atomic numbers relative to the matrix elements Si ($Z = 14$), O ($Z = 8$), and N ($Z = 7$). Figure 8 shows images recorded for two directions perpendicular to a grain–intergranular film and to a grain–glassy pocket. Averaging of these images has been performed to compensate for the effects of specimen drift during the ~ 1 min scan time.

The structure of the $\{001\}$ -oriented Si_3N_4 crystal is imaged on one side of the interface (lower half in the images in Figure 8), but no lattice contrast is visible on the other side, as the crystal is either not aligned to a zone axis (in the case of the misoriented grain) or the structure is amorphous (in the case of the glass pocket). Within the intergranular film adjacent to the Si_3N_4 crystal, the rare-earth atom locations are imaged as bright spots. From the positions of the rare-earth atoms measured from two independent projections of the interface, the cation positions in all three dimensions have been determined, as illustrated schematically in Figure 8 and tabulated in Reference 19. These positions clearly differ for the two rare-earth elements illustrated, but for either element, they are independent of the nature of the interface (intergranular film or glassy phase).

Case Studies in Materials with Aberration-Corrected CTEM Nanoparticles

One of the major benefits of spherical aberration correction in CTEM is the reduction in image artifacts due to contrast

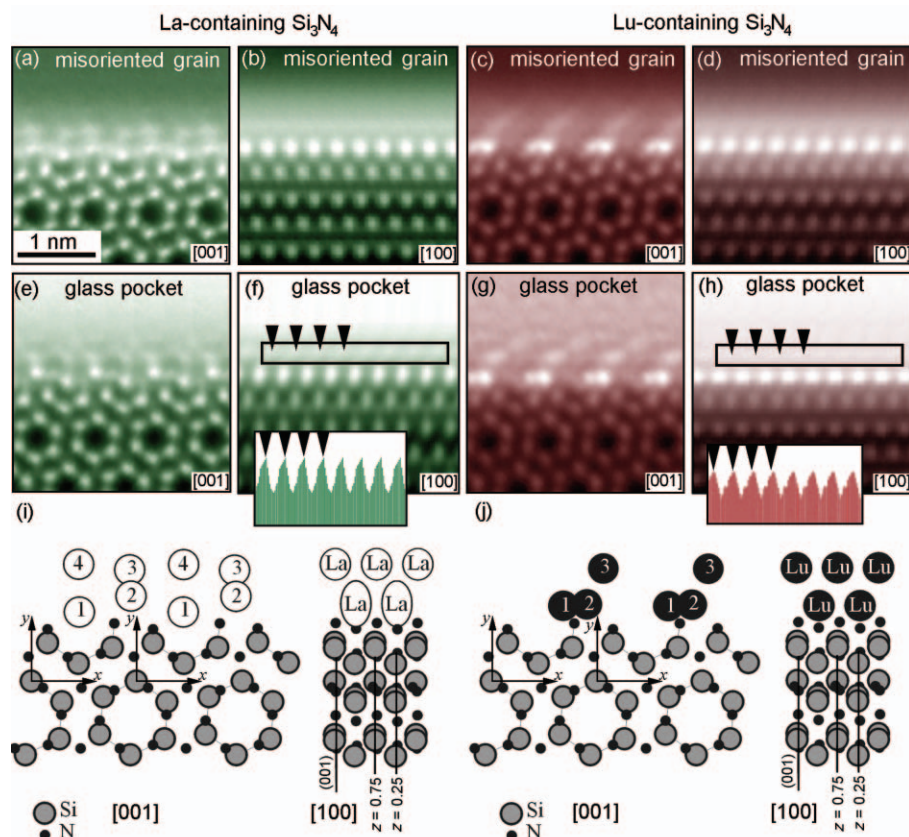


Figure 8. Unwarped and averaged high-angle annular dark-field STEM images of $\{100\}$ crystal–amorphous interfaces in rare-earth-containing Si_3N_4 . (a),(b) Crystal–intergranular film interface in La-containing Si_3N_4 viewed parallel to $[001]$ and $[100]$, respectively. (c),(d) Crystal–intergranular film interface in Lu-containing Si_3N_4 viewed parallel to $[001]$ and $[100]$, respectively. (e)–(h) Images corresponding to (a)–(d) of crystal–glassy pocket interfaces for both La- and Lu-containing samples. The insets in (f) and (h) show the intensity modulations in the bounded regions marked. (i),(j) Schematic representations of the interfacial structure projected parallel to both $[001]$ and $[100]$ for La- and Lu-containing specimens, respectively. The numbers 1, 2, 3, and 4 refer to different rare-earth atom sites within each model. (After Winkelmann et al., reproduced from Reference 19.)

delocalization. This brings particular benefits in the imaging of interfaces and surfaces. For surfaces, this is of particular benefit in untangling the contrast of nanoparticles, including those used in catalysis, from the generally amorphous or quasi-amorphous support material.²² Aberration-corrected CTEM has also been used to determine that nanoscale PbSe dots grown on wurzite CdS and CdSe rods²³ exhibit the rock-salt structure and to image oxygen atoms at $\{100\}$ surfaces of magnesium oxide.²⁴

Figures 9a and 9b show a series of images of a nanocrystalline Pt catalyst particle supported on partially graphitized carbon recorded for several defocus values in the presence of spherical aberration and also with the spherical aberration corrected. The uncorrected images (Figure 9a) show extensive contrast delocalization at

the particle surfaces, which is largely removed when the spherical aberration is corrected (Figure 9b).

From the aberration-corrected images, it is possible to determine the detailed surface structure of the particles, and in particular, the image shows several incomplete surface layers on both $\{111\}$ and $\{100\}$ facets that are significant in terms of the catalytic activity and selectivity of this material. The correction of spherical aberration also leads to a reduced depth of field, and this provides additional valuable information about the three-dimensional relationship between the particle and support. Figure 9b clearly shows this effect in which the contrast of the particle remains relatively unchanged with defocus, whereas the contrast arising from the support material that lies at a different height changes rapidly with defocus.

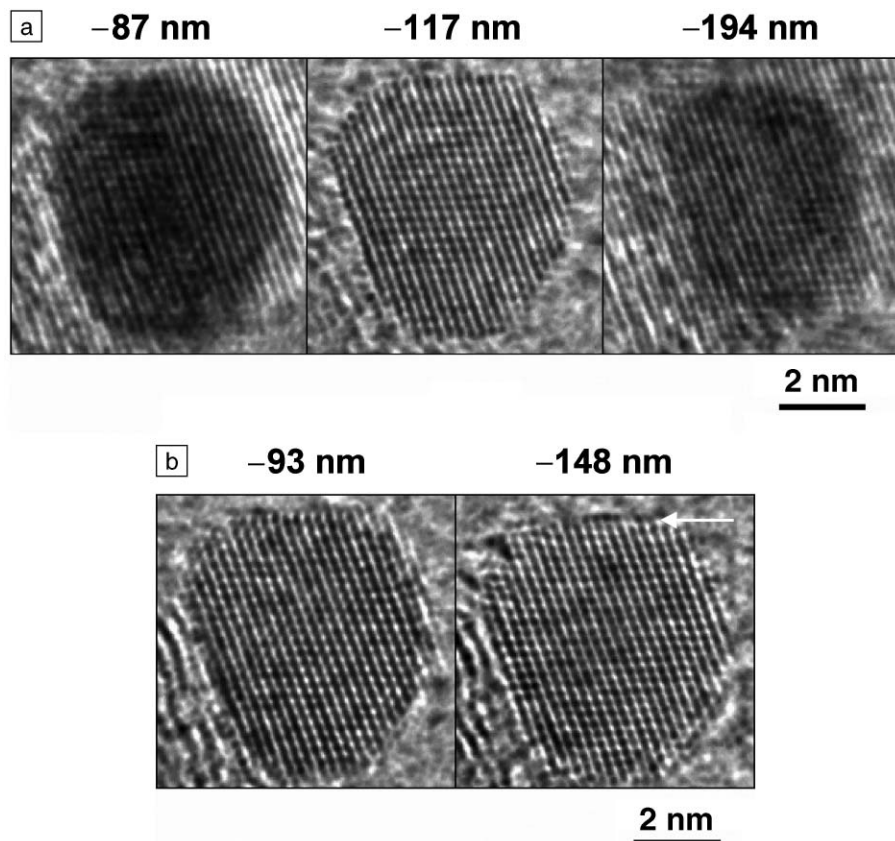


Figure 9. (a) Through-focal series of images of a nanocrystalline Pt particle supported on partially graphitized carbon with a spherical aberration of $450 \mu\text{m}$. (b) Equivalent focal series of the same particle after aberration correction with a spherical aberration of $-20 \mu\text{m}$. In both (a) and (b), defocus values are indicated, with negative values corresponding to underfocus. In (a), extensive contrast delocalization as a function of defocus is observed, which is eliminated in (b). A partially complete surface layer is marked with an arrow in (b).

Defects in Semiconductors

Semiconductors have been extensively studied by high-resolution CTEM from its earliest days, and aberration correction now enables the direct imaging of individual atomic columns in several projections at intermediate voltages where radiation damage is less important. This has enabled characterization, at the atomic level, of many defects. Preliminary work on $\text{SiO}_2/\text{Si}(100)$ interfaces shows that the elimination of image delocalization offers particular advantages, and prospects for imaging oxygen atoms at these interfaces have been explored.²⁵

Stacking faults in $\text{Si}_{1-x}\text{Ge}_x$ have also been examined by aberration-corrected CTEM and compared with Z-contrast images taken by STEM.²⁶ This work makes the important point that, even when the microscope aberrations are corrected, the quality of the specimen is still crucial: in this case, the presence of a stacking fault leads to localized tilting of the lattice around the fault away from the zone axis.

The combination of exit-plane wave function reconstruction and aberration correction has been applied to defects in GaAs.²⁷ Optimum-defocused, aberration-corrected images show the defects without delocalization effects, but the reconstruction of the exit wave from a series of images produces an improved signal-to-noise ratio, as shown in Figure 10. Detailed analysis of the image contrast in the GaAs matrix has also allowed the polarity of the material to be determined such that a full identification of the individual atoms in a multiple stacking fault and bounding dislocation was possible.

Future Directions

Aberration correction in both conventional transmission electron microscopy and scanning transmission electron microscopy increases the spatial resolution by allowing the objective lens aperture to be increased. As in a camera, this results in a reduced depth of focus that decreases as the square of the aperture angle, whereas

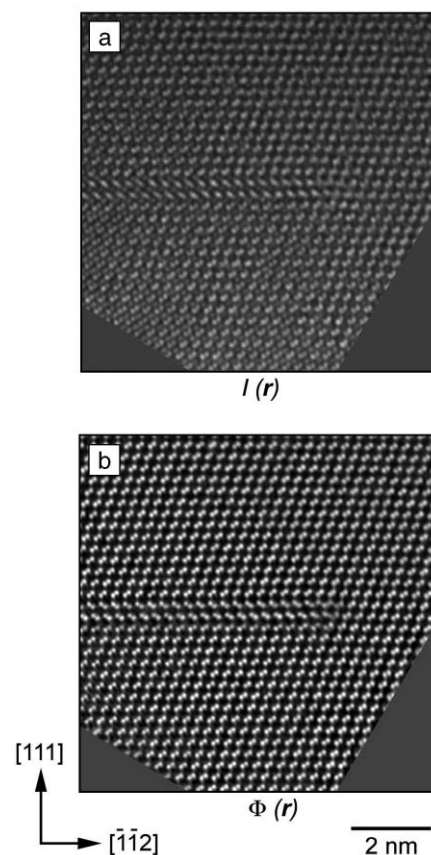


Figure 10. Multiple stacking fault in GaAs laterally bound by a partial dislocation. (a) Optimum defocus image, $I(r)$. (b) Reconstructed exit plane phase, $\Phi(r)$, showing enhanced contrast and lower noise levels. (Reproduced with permission from Reference 27.)

the lateral resolution, which has been the main motivation for aberration correction, improves only linearly with aperture angle. Depth resolution on an aberration-corrected 300-kV scanning transmission electron microscope is at the nanometer scale, and it is now possible to optically slice through a sample simply by changing the objective lens focus. Accordingly, a through-focal image series now becomes a through-depth series that can be reconstructed to give a three-dimensional data set²⁸ in a similar manner as that used in confocal optical microscopy. Although electron channeling complicates this approach, in a thin, amorphous sample the technique provides single-atom sensitivity in each image. Recently, individual Hf atoms in a sub-nm-wide region of SiO_2 in a high- κ device structure have been located to a precision of about $0.1 \text{ nm} \times 0.1 \text{ nm} \times 1 \text{ nm}$,²⁹ as illustrated in Figure 11.

At the present time, spherical aberration has been successfully corrected in

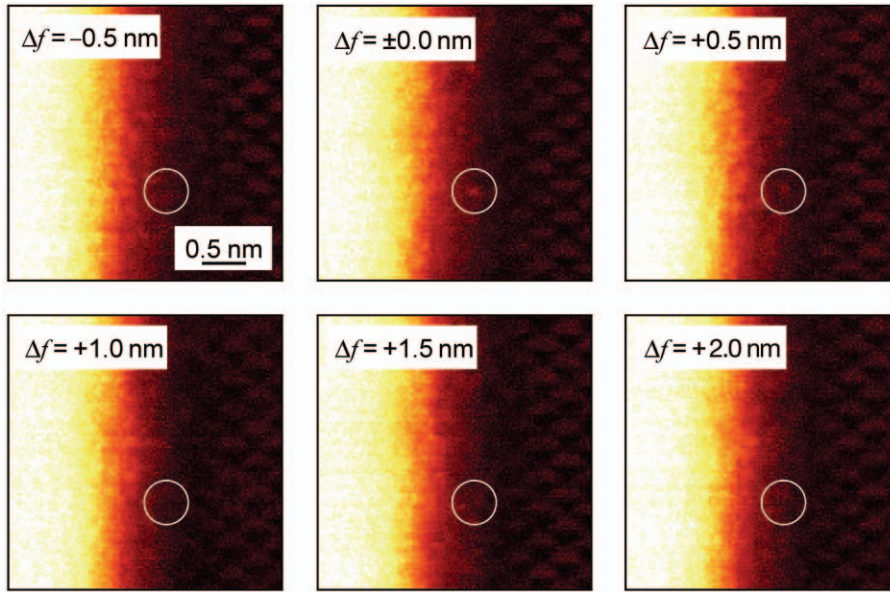


Figure 11. A series of frames from a through-focal series of images, recorded in defocus steps (Δf) of 0.5 nm, showing the appearance and disappearance of an individual Hf atom (circled) in a thin layer of SiO_2 between the HfO_2 dielectric region (left) and the Si gate region (right). (Courtesy of K. van Benthem.)

CTEM, improving the point resolution to the information limit. In order to extend the information limit itself, there are two possibilities, both of which are actively being pursued. The first possibility is to reduce the energy spread of the electrons (and thus improve the limit set by temporal coherence) by replacing the standard thermally assisted Schottky field-emission gun (FEG) with a cold FEG, or by monochromating the electron beam. The second is to correct the chromatic aberration of the objective lens³⁰ using a complex combination of magnetic and electrostatic multipole elements. An improved information limit will allow not only greater detail and precision to be obtained in the analysis of the atomic structure of materials but will also permit the use of large-gap pole pieces without the constraint of minimizing the spherical and chromatic aberration. These larger gap lenses will in turn allow the use of a wider range of specialized specimen holders for *in situ* experiments and measurements with dynamic observation.

Acknowledgments

Work at ORNL was possible thanks to the collaboration of A.R. Lupini, A. Borisevich, Y. Peng, M.P. Oxley, K. van Benthem, M.F. Chisholm, P.D. Nellist, O.L. Krivanek, N. Dellby, M.F. Murfitt, Z.S. Szilagy, S.F. Findlay, L.J. Allen, J. Santamaria, D.G. Mandrus, R. Jin, and S.T. Pantelides, and was supported by the

Laboratory Directed Research and Development Program of ORNL, managed by UT-Battelle LLC for the U.S. Department of Energy under contract DE-AC05-000R22725. Work at the University of Oxford was possible due to collaborations with D.J.H. Cockayne, G. Winkelmann, C. Dwyer, L.Y. Chang, H. Sawada, R. Dunin-Borkowski, and L. Cervera and has been supported by the EPSRC, the Leverhulme Trust, JEOL, and the DTI.

References

1. R.P. Feynman, <http://www.zyvex.com/nanotech/feynman.html> (accessed December 2005).
2. H. Rose, *Ultramicroscopy* **56** (1994) p. 11.
3. Nion Co. Home Page, <http://www.nion.com/> (accessed December 2005).
4. CEOS-Corrected Electron Optical Systems GmbH Home Page, <http://www.ceos-gmbh.de/> (accessed December 2005).
5. J. Zach and M. Haider, *Nucl. Inst. Meth.* **A363** (1995) p. 316.
6. C.L. Jia, M. Lentzen, and K. Urban, *Science* **299** (2003) p. 870.
7. J.L. Hutchison, J.M. Titchmarsh, D.J.H. Cockayne, R.C. Doole, C.J.D. Hetherington, A.I. Kirkland, and H. Sawada, *Ultramicroscopy* **103** (2005) p. 7.
8. M. Lentzen, B. Jahnen, C.L. Jia, A. Thust, K. Tillmann, and K. Urban, *Ultramicroscopy* **92** (2002) p. 233.
9. A.I. Kirkland and R.R. Meyer, *Microsc. Microanal.* **10** (2004) p. 401.
10. M. Varela, S.D. Findlay, A.R. Lupini, H.M. Christen, A.Y. Borisevich, N. Dellby, O.L. Krivanek, P.D. Nellist, M.P. Oxley, L.J. Allen,

and S.J. Pennycook, *Phys. Rev. Lett.* **92** 095502 (2004).

11. N.D. Browning, J. Yuan, and L.M. Brown, *Physica C* **202** (1992) p. 12.
12. N.D. Browning, M.F. Chisholm, S.J. Pennycook, D.P. Norton, and D.H. Lowndes, *Physica C* **212** (1993) p. 185.
13. M. Varela, A.R. Lupini, V. Pena, Z. Sefrioui, I. Arslan, N.D. Browning, J. Santamaria, and S.J. Pennycook, "Direct measurement of charge transfer phenomena at ferromagnetic/superconducting oxide interfaces," preprint, condmat/0508564 (accessed December 2005).
14. E. Dagotto, T. Hotta, and A. Moreo, *Phys. Rep.* **344** (2001) p. 1.
15. S. Jin, T.H. Tiefel, M. McCormack, R.A. Fastnacht, R. Ramesh, and L.H. Chen, *Science* **264** (1994) p. 413.
16. R. Von Helmolt, J. Wecker, B. Holzapfel, L. Schultz, and K. Samwer, *Phys. Rev. Lett.* **71** (1993) p. 2331.
17. H. Woo, T.A. Tyson, M. Croft, S.W. Cheong, and J.C. Woicik, *Phys. Rev. B* **63** 134412 (2001).
18. M. Varela et al. (2005) unpublished.
19. G.B. Winkelmann, C. Dwyer, T.S. Hudson, D. Nguyen-Manh, M. Doeblinger, R.L. Satet, M.J. Hoffmann, and D.J.H. Cockayne, *Appl. Phys. Lett.* **87** 061911 (2005).
20. N. Shibata, S.J. Pennycook, T.R. Gosnell, G.S. Painter, W.A. Shelton, and P.F. Becher, *Nature* **428** (2004) p. 730.
21. A. Ziegler, J.C. Idrobo, M.K. Cinibulk, C. Kisielowski, N.D. Browning, and R.O. Ritchie, *Science* **306** (2004) p. 1768.
22. L. Cervera Gontard, L-Y Chang, R.E. Dunin-Borkowski, A.I. Kirkland, C.J.D. Hetherington, and D. Ozkaya, *Inst. Phys. Conf. Ser. EMAG 05* (2005) in press.
23. S. Kudara, L. Carbone, M.F. Casula, R. Cingolani, A. Falqui, E. Snoeck, W.J. Parak, and L. Manna, *Nano Lett.* **5** (2005) p. 445.
24. N. Tanaka, J. Yamasaki, and T. Kawai, Extended abstract of a paper presented at Microscopy and Microanalysis 2004 (Savannah, Georgia, August 1-5, 2004).
25. N. Tanaka, J. Yamasaki, K. Usuda, and N. Ikarashi, *J. Electron Microsc.* **52** (2003) p. 69.
26. J. Yamasaki, T. Kawai, and N. Tanaka, *J. Electron Microsc.* **53** (2004) p. 129.
27. K. Tillmann, A. Thust, and K. Urban, *Microsc. Microanal.* **10** (Cambridge UP, 2004) p. 185.
28. S.J. Pennycook, A.R. Lupini, A. Borisevich, Y. Peng, and N. Shibata, *Microsc. Microanal.* **10** (Suppl. 1.2) (2004) p. 1172.
29. K. van Benthem, A.R. Lupini, M. Kim, H.S. Baik, S. Doh, J.-H. Lee, M.P. Oxley, S.D. Findlay, L.J. Allen, and S.J. Pennycook, *Appl. Phys. Lett.* **87** 034104 (2005).
30. H. Rose, *Nucl. Instrum. Methods Phys. Res. A* **519** (2004) p. 12.



Stephen J. Pennycook is a corporate fellow in the Condensed Matter Sciences Division at Oak Ridge National Laboratory and leader of the Electron Microscopy Group (stem.ornl.gov). His current research interests focus on

the development of Z-contrast scanning transmission electron microscopy and electron energy loss spectroscopy with sub-angstrom resolution, and their applications to materials science, catalysis, biology, and nanoscience. He is a recipient of the Materials Research Society Medal and the Thomas Young Medal of the Institute of Physics.

Pennycook can be reached at Oak Ridge National Laboratory, Condensed Matter Sciences Division, PO Box 2008, Oak Ridge, TN 37831-6030 USA; tel. 865-574-5504, fax 865-574-4143, and e-mail pennycooks@ornl.gov.



Maria Varela is an Electron Microscopy Group research staff member in the Condensed Matter Sciences Division at Oak Ridge National Laboratory. She received her PhD degree in solid-state physics from the Complutense University of

Madrid, Spain. She has wide experience in the growth, physical properties, measurements, and structural characterization of thin films, in particular, high-temperature superconducting thin films and superlattices. Her current research interests focus on the study of the properties of com-

plex oxide thin films and interfaces by means of aberration-corrected Z-contrast scanning transmission electron microscopy and electron energy loss spectroscopy with sub-angstrom resolution. She has authored over 60 papers in journals such as the Journal of Materials Research, Physical Review Letters, and Nature. She is also a recipient of the Royal Spanish Physics Society Award for Novel Researchers and the Oak Ridge National Laboratory Wigner Fellowship.

Varela can be reached at Condensed Matter Sciences Division, Oak Ridge National Laboratory, PO Box 2008, Bldg. 3025M, MS 6031, Oak Ridge, TN 37831-6031 USA; tel. 865-574 6287, fax 865-574 4143, and e-mail mvarela@ornl.gov.



Crispin J.D. Hetherington is a research fellow in the Department of Materials at Oxford University, where he also earned his undergraduate and DPhil degrees. He has worked in a number of electron microscopy facilities, including the National Center for Electron Microscopy in Berkeley, Calif., and Sheffield and Cambridge in the United Kingdom. His research interests are the characteriza-

tion of interfaces and materials at the atomic level through the use of aberration-corrected microscopy.

Hetherington can be reached at University of Oxford, Department of Materials, Parks Rd., Oxford OX1 3PH, United Kingdom; tel. 44-1865-283740, fax 44-1865-848790, and e-mail crispin.hetherington@materials.ox.ac.uk.



Angus I. Kirkland has been a professor of materials at the University of Oxford since 2005. He was awarded his MA and PhD degrees from the University of Cambridge. His current research interests include applications of aberration-corrected high-

resolution transmission electron microscopy for structural studies of nanomaterials, the design of direct electron detectors, and the development of computational image processing and theory for enhancing resolution in TEM. He is a fellow of the Institute of Physics and of the Royal Society of Chemistry.

Kirkland can be reached at the University of Oxford, Department of Materials, Parks Rd., Oxford OX1 3PH, United Kingdom; e-mail angus.kirkland@materials.ox.ac.uk.

Chapter Challenge ²⁰⁰⁶

—an event designed to spark a little
“friendly competition” among MRS Chapters.

The premise is simple. We've come up with a theme, **Biology—The Next Frontier of Materials Science and Engineering**, and we want to see just what your members can do with it.

That's it. We're giving you the theme and not much more. Your challenge is to come up with a creative program or activity that relates to biology and materials science & engineering... and then make it happen!

Details for the competition can be found on our Web site:
www.mrs.org/university/2006challenge

So get your Chapter together and set the creative juices flowing. It's a great way to energize your membership, increase student involvement, and showcase your Chapter.

Deadline for entries is **April 1, 2006**.

The winning Chapter will be announced May 1, 2006 and will be featured in a summer issue of the *MRS Bulletin*.

Don't lose another minute. The Chapter Challenge starts NOW!

JANIS

CRYOGENIC WAFER PROBE STATIONS



- DC to 60 GHz
- 3.2 K to 450 K
- Imaging with microscopes and cameras
- Two to six probe stations
- Cooling options: liquid helium, liquid nitrogen, or cryogen free

Janis Research Company

2 Jewel Drive Wilmington, MA 01887 USA
TEL +1 978 657-8750 FAX +1 978 658-0349 sales@janis.com
Visit our website at www.janis.com.

For more information, see <http://advertisers.mrs.org>